Pakistan Veterinary Journal

ISSN: 0253-8318 (PRINT), 2074-7764 (ONLINE)
DOI: 10.29261/pakvetj/2025.314

RESEARCH ARTICLE

Artificial Intelligence-Assisted Estimation of the Center of Rotation of Angulation (CORA) in Canine Forelimb Radiographs

Seoro Park[1†], Taehun Kim[2†], HyunGyu Lee[3], Kichang Lee[1] and Hakyoung Yoon[1*]

[1]Department of Veterinary Medical Imaging, College of Veterinary Medicine, Jeonbuk National University, Iksan-si, Republic of Korea; [2] Department of Electrical and Computer Engineering, Inha University, Incheon, Republic of Korea; [3] College of Medicine, Inha University, Incheon, Republic of Korea. †These authors contributed equally to this work and share first authorship
*Corresponding author: knighttt7240@gmail.com

ARTICLE HISTORY (25-849)

Received:	September 07, 2025
Revised:	November 13, 2025
Accepted:	November 16, 2025
Published online:	December 09, 2025

Key words:
Artificial intelligence
Angular limb deformity
Chondrodystrophic breed
Dog
Radius

ABSTRACT

Angular limb deformity (ALD) in the canine forelimbs requires precise quantitative evaluation for accurate diagnosis and optimal surgical planning. The Center of Rotation of Angulation (CORA) methodology, though accurate, is limited by its time consumption and inter-observer variability; therefore, we developed an AI-based model to automatically predict the CORA point and six angular parameters using antebrachial radiographs. A total of 504 radiographs from 126 dogs (54 chondrodystrophic and 72 non-chondrodystrophic; mean age: 8.62 years) taken between January 2018 and July 2024 were retrospectively analyzed. Radius segmentation was performed using a VGG11-based U-Net11 model, and key points for joint orientation lines (JOLs) were identified using a High-Resolution Network (HRNet). A rule-based algorithm estimated the proximal and distal radial anatomical axes (RAAs) and defined the CORA point. The deep learning model performance was evaluated using the Intersection over Union (IoU), Dice Similarity Coefficient (DSC), and Normalized Mean Error (NME). The segmentation accuracy reached IoUs of 0.926 (frontal) and 0.919 (sagittal), with DSCs of 0.961 and 0.958, respectively. The NME values were 0.0061 (frontal) and 0.0047 (sagittal). The CORA predictions closely matched those of veterinarians, particularly in chondrodystrophic breeds. Intraclass correlation coefficients (ICC) exceeded 0.9 for most angle measurements. The average inference time was 1.19 seconds per image. This automated approach offers a fast and consistent evaluation of the CORA and related angles, supporting the clinical assessment of ALD while minimizing inter-observer variability.

To Cite This Article: Park S, Kim T, Lee H, Lee K and Yoon H, 2025. Artificial intelligence-assisted estimation of the center of rotation of angulation (cora) in canine forelimb radiographs. Pak Vet J. http://dx.doi.org/10.29261/pakvetj/2025.314

INTRODUCTION

Angular limb deformities (ALDs) arise from congenital malformations, physical trauma, nutritional imbalances, and other factors that cause growth plate delays (Marcellin-Little, 2020; Kwon *et al.*, 2022). Particularly, chondrodystrophic breeds are predisposed to ALDs owing to disproportionate long bone growth, often resulting from premature closure of the distal ulnar growth plate (Parker *et al.*, 2009; Fox, 2010; Pulkkinen *et al.*, 2020). ALDs affecting the radius and ulna are common in dogs (Emery, 2016). Radial deformities include valgus and varus, which are identified in the craniocaudal views, and procurvatum and recurvatum, which are observed in the mediolateral views (Emery, 2016). Accurate correction requires evaluation using the center of rotation of the angulation (CORA) methodology based on at least two radiographic views.

The CORA methodology is a quantitative approach to evaluate bone deformities and determine the optimal osteotomy site and correction strategy (Fox *et al.*, 2006; Beale, 2010; Muniyya, 2023). It was initially proposed in human orthopedic surgery in 2006 but has been increasingly adopted in veterinary orthopedics for the correction of limb deformities (Paley, 2014). The CORA point is defined as the intersection between the normal anatomical axis and the deformed axis of the bone, and performing osteotomy at this location allows correction without introducing translational deformities (Fox *et al.*, 2006; Kim *et al.*, 2017). Precise identification of the CORA point directly influences surgical outcomes because inaccurate localization can lead to complications such as malunion or nonunion. Therefore, the meticulous application of the CORA methodology is essential to optimize the efficacy of corrective surgery and enhance patient prognosis.

The CORA methodology differentiates between uniapical and biapical/multiapical deformities, influencing CORA points and surgical techniques (Fox *et al.*, 2006; Knapp *et al.*, 2016). Uniapical deformities have a single apex, allowing correction at one CORA point. Biapical or multiapical deformities involve multiple CORA points and require individual corrections. Complete correction may require multiple osteotomies (Dismukes *et al.*, 2008).

The methodology measures four angular parameters: medial proximal radial angle (MPRA), lateral distal radial angle (LDRA), proximal cranial radial angle (PCRA), and distal caudal radial angle (DCRA). In the craniocaudal view, MPRA is the angle between the elbow joint orientation line (JOL) and RAA, while LDRA is between the carpal JOL and RAA. Frontal plane alignment (FPA) is defined as |MPRA − LDRA|, with a normal range of 0–8° and a mean of 2.7°; higher values indicate valgus or varus deformities (Fox *et al.*, 2006; Duncan *et al.*, 2022). In the lateral view, PCRA forms between elbow JOL and proximal RAA, DCRA between carpal JOL and distal RAA. Sagittal plane alignment (SPA) is defined as PCRA − DCRA, with a normal range of 8–35° and a mean of 25.2°; deviations indicate procurvatum or recurvatum (Fox *et al.*, 2006; Duncan *et al.*, 2022). The acute angle between proximal and distal RAAs is θ. Procurvatum is calculated as θ + (90° − anatomic caudal proximal radial angle [aCdPRA]) + (90° − anatomic caudal distal radial angle [aCdDRA]), with breed-specific thresholds (Fasanella *et al.*, 2010; Fox and Tomlinson, 2012; Knapp *et al.*, 2016).

Currently, radial deformities and CORA points are identified manually using radiographic or CT images (Fox *et al.*, 2006; Dismukes *et al.*, 2008; Kroner *et al.*, 2017). This approach is time-consuming and varies between observers, necessitating an automated deep-learning system.

We hypothesized that deep learning could be used to develop an AI-based evaluation model capable of automatically predicting the radial axes, measuring six clinically relevant angles, and identifying CORA points from canine forelimb radiographs. We anticipated that this approach would overcome the limitations of manual measurement and contribute to more consistent and objective clinical decision-making. Such automation could improve practical clinical workflow by enabling faster assessments and reducing the burden of repeated measurements during preoperative planning.

MATERIALS AND METHODS

Data collection and extraction: This study was approved by the Animal Care and Use Committee of Jeonbuk National University, Iksan, Jeollabuk-do, Republic of Korea (approval no. JBNU 2023-168). In this study, 126 dogs, comprising 51 chondrodystrophic and 75 non-chondrodystrophic breeds, were selected (Table 1). Classification was based on previous studies (Smolders et al., 2013; Kranenburg et al., 2013). The average age was 8.62±4.33 years, with a mean weight of 7.85±5.38 kg. A total of 66 females and 60 males were included (Table 2).

Table 1: Distribution of experimental dogs according to the chondrodystrophic and non-chondrodystrophic breeds

Non-chondrodystrophic breed (75 dogs)	Chondrodystrophic breed (51 dogs)
Maltese (17)	Welsh Corgi (22)
Pomeranian (15)	Dachshund (8)
Poodle (14)	Pekingese (6)
Mixed (12)	Bichon Frise (4)
Yorkshire Terrier (5)	Shih Tzu (4)
Jindo (4)	French Bulldog (3)
Spitz (3)	American Cocker Spaniel (2)
Golden Retriever (2)	Beagle (1)
Cane Corso (1)	Boxer (1)
Miniature Pinscher (1)	
Mini Pin (1)	

Table 2: Demographics by breed (age, body weight: mean±SD; sex: n (%))

Number		Non-chondrodystrophic breed (75 dogs)	Chondrodystrophic breed (51 dogs)	Total (126 dogs)
Age (years)		8.81±4.31	8.35±4.39	8.62±4.33
BW (kg)		6.15±4.54	10.34±5.59	7.85±5.38
Sex (%)	Female	39 (30.95)	27 (21.42)	66 (52.38)
	Male	36 (28.57)	24 (19.04)	60 (47.62)

SD, standard deviation; BW, body weight

Radiographic images (504) in sagittal and frontal planes of both forelimbs of 126 dogs presenting to Jeonbuk National University, Bundang Leaders Animal Hospital, Seongbuk VIP Animal Hospital, and Nell Animal Hospital between January 2018 and July 2024 were retrospectively reviewed. The sample size was comparable to or larger than those of previous studies assessing similar angular parameters in canine forelimb radiographs. Thus, the dataset was considered sufficient for reliable statistical comparison among six parameters. Similar imaging settings were applied across hospitals, and inter-institutional variation was minimized by radiologist review. The overall study population and dataset construction are schematically illustrated in Fig. 1. Digital images were evaluated using a DICOM workstation, while conventional films were assessed with a DICOM viewer. Evaluations were performed in sagittal and frontal planes. Images were independently reviewed in randomized order by two authors.

The study included dogs ≥2 years old with mature forelimb skeletons. All dogs were clinically normal without lameness or pain. Dogs with surgical devices, fractures, biapical or multiapical deformities identified during pre-evaluation, inaccurate radiographic positioning, or images showing only one joint relative to the radius (n=129) were excluded (Fig. 1).

Manual labelling: Radius drawing and JOL keypoint annotation: Two veterinarians labeled 375 bilateral forelimb radiographs using the MediLabel software (version 1.0.0, Yozma Group, Seoul, Korea) on a standard workstation (Intel Core i7, 32 GB RAM, NVIDIA GPU) (Fig. 1). For radius segmentation, the region of interest was drawn along the radius boundary.

For keypoint detection, four anatomical points were annotated on frontal and sagittal planes (Fig. 2A, D). In the frontal plane, these points defined the JOL. According to previous studies, the proximal JOL refers to the humeroradial articular surface, and the distal JOL refers to the radiocarpal articular surface (Paley, 2014; Muniyya, 2023). However, to train a deep learning model, clearly defined anatomical landmarks are required. We defined the proximal JOL as the line connecting the lateral aspect of the radial head and medial coronoid process of the ulna (Kwon *et al*., 2022). When the medial coronoid process was not visible due to radius and ulna superimposition, the medial aspect of the radial head was marked. The distal JOL was defined as the line connecting medial and lateral points at the intersection of distal radius and carpal bones. The four key points in the frontal plane were the lateral aspect of the radial head, medial coronoid process of the ulna, and medial and lateral crossing points between the distal radius and carpal bones (Fig. 2A).

In the sagittal plane, the JOLs were defined using four key points: the cranial and caudal aspects of the radial head (proximal JOL) and the distal radius (distal JOL) (Fig. 2D).

CORA point annotation and angle measurement: To evaluate CORA point prediction accuracy between the AI model and veterinarians, 9 chondrodystrophic and 9 non-chondrodystrophic dogs were selected (Fig. 1). A total of 72 radiographic images from both forelimbs in two planes from 18 dogs were labeled by five veterinarians (3 third-year and 2 second-year graduate students in veterinary radiology) using CORA methodology.

CORA point determination was required the RAA, defined as a line through the bone shaft center (Paley, 2014; Knapp *et al*., 2016; Kwon *et al*., 2022). On frontal and sagittal planes, veterinarians drew proximal RAA along the proximal radial shaft center and distal RAA along the distal shaft (Knapp *et al*., 2016). The intersection formed the CORA point, yielding six angular parameters.

In the frontal plane, the medial proximal radial angle (MPRA) was measured as the medial angle between the proximal JOL and the proximal RAA, and the lateral distal radial angle (LDRA) was measured as the lateral angle between the distal JOL and the distal RAA (Fig. 2B). The angle formed by the intersection of the two RAAs was termed the frontal intersection angle (FIA). In the sagittal plane, cranial proximal radial angle (CrPRA) was defined as the angle between proximal JOL and proximal RAA facing cranially, while caudal distal radial angle (CdDRA) was the caudal-facing angle between distal JOL and distal RAA (Fig. 2E). The angle of intersection between proximal and distal RAAs was termed the sagittal intersection angle (SIA).

CORA estimation method: The CORA estimation method comprised feature extraction using deep learning models and RAA/CORA estimation (Fig. 3). A segmentation network delineated the radius from X-ray images, and a keypoint detection network localized anatomical landmarks defining JOLs for calculating anatomical angles. As RAA and CORA involved subjective judgment, we proposed the Radius Anatomical Geometry Estimator for CORA (RAGE-CORA), a segmentation-based algorithm estimating RAA and CORA through geometric analysis. RAGE-CORA determined mid-diaphyseal contour, detected curvature peaks, and estimated RAA through contour linearization. CORA and angular measurements were obtained by intersecting estimated RAA with predicted keypoint-defined JOLs.

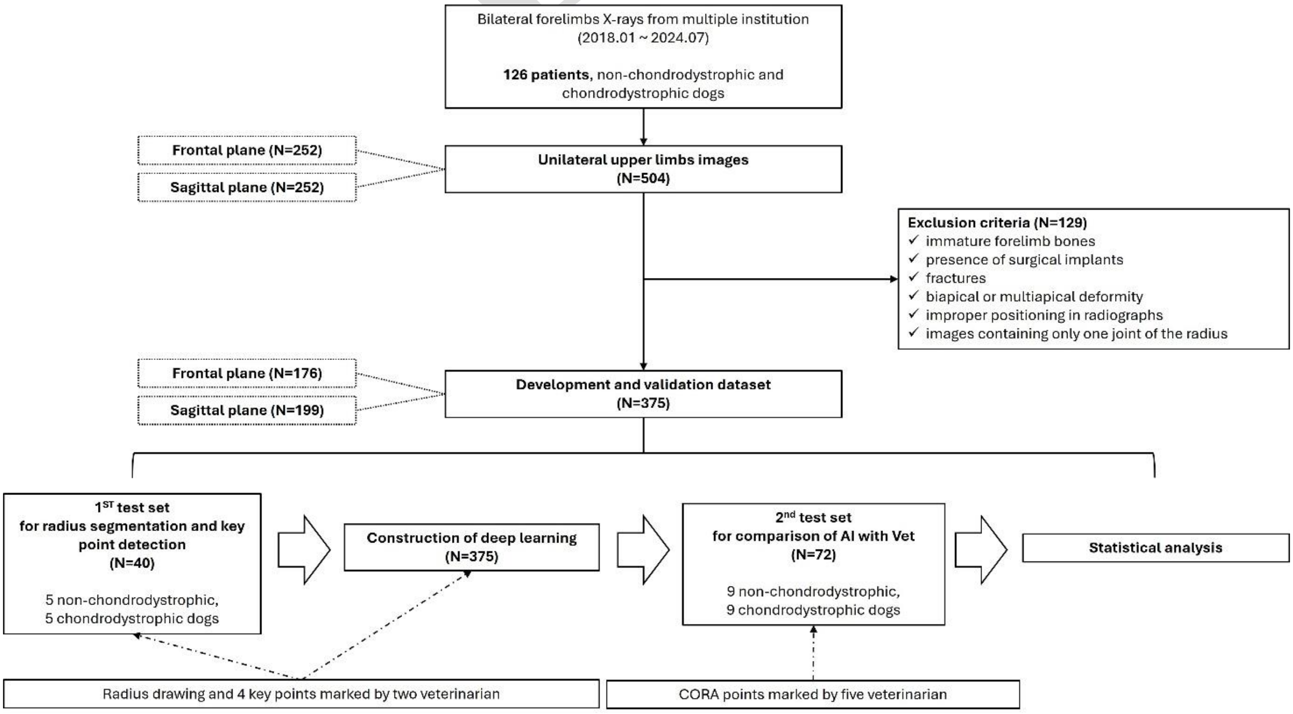

Fig. 1: Overview of the study population and dataset construction. Bilateral forelimb radiographs (N=504) from 126 dogs were collected. Following the application of exclusion criteria (N=129), deep learning was conducted on the remaining cases (N=375). A first test set (N=40) was used for radial segmentation and key point detection, while a second test set (N=72) was used to compare CORA point prediction between veterinarians and AI. Test cases were randomly selected.

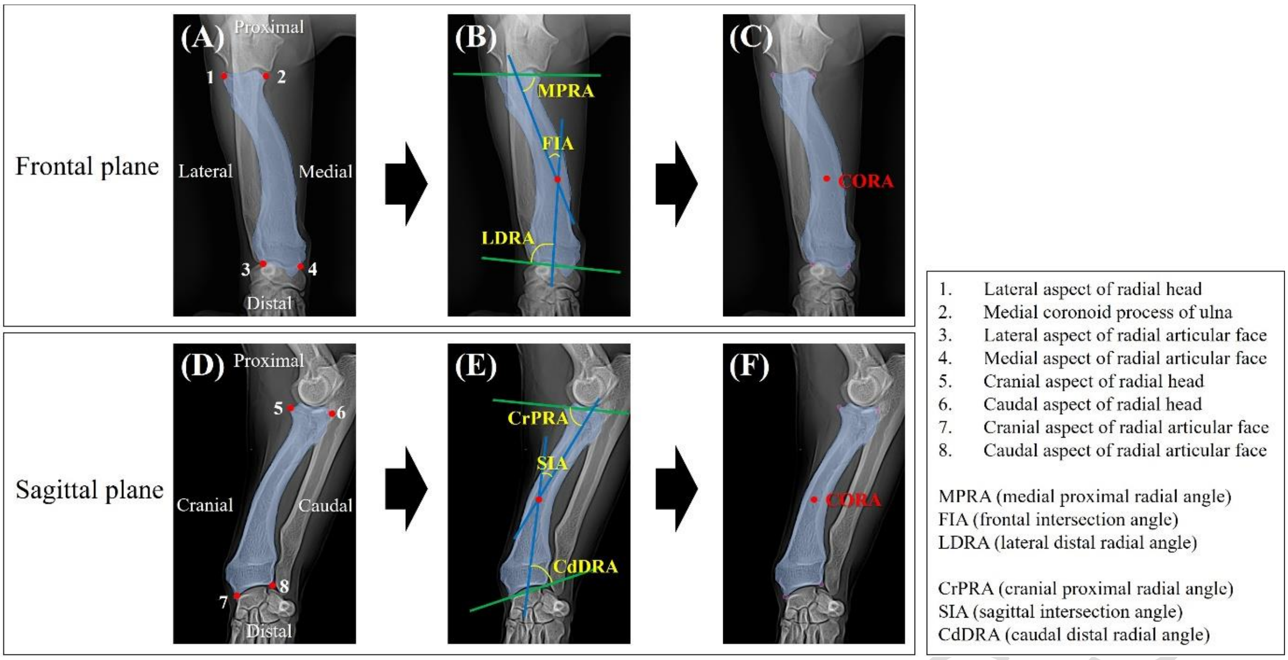

Fig. 2: Manual measurement of CORA point and angular parameters in the frontal (A-C) and sagittal (D-F) planes. Frontal plane: (A) Anatomical landmarks 1–4 for joint orientation lines (definitions in the lower-right box). (B) Green line: joint orientation lines (JOL) (proximal/distal); blue line: radial anatomical axes (RAA) (proximal/distal). Angular parameters—MPRA (proximal JOL–proximal RAA), FIA (proximal RAA–distal RAA), LDRA (distal RAA–distal JOL). (C) Red dot: CORA point. Sagittal plane: (D) Anatomical landmarks 5–8 (definitions in the lower-right box). (E) Angular parameters CrPRA (proximal JOL–proximal RAA), SIA (proximal RAA–distal RAA), CdDRA (distal RAA–distal JOL). (F) Red dot: CORA point. The full names of the angular parameters are provided in the lower-right box.

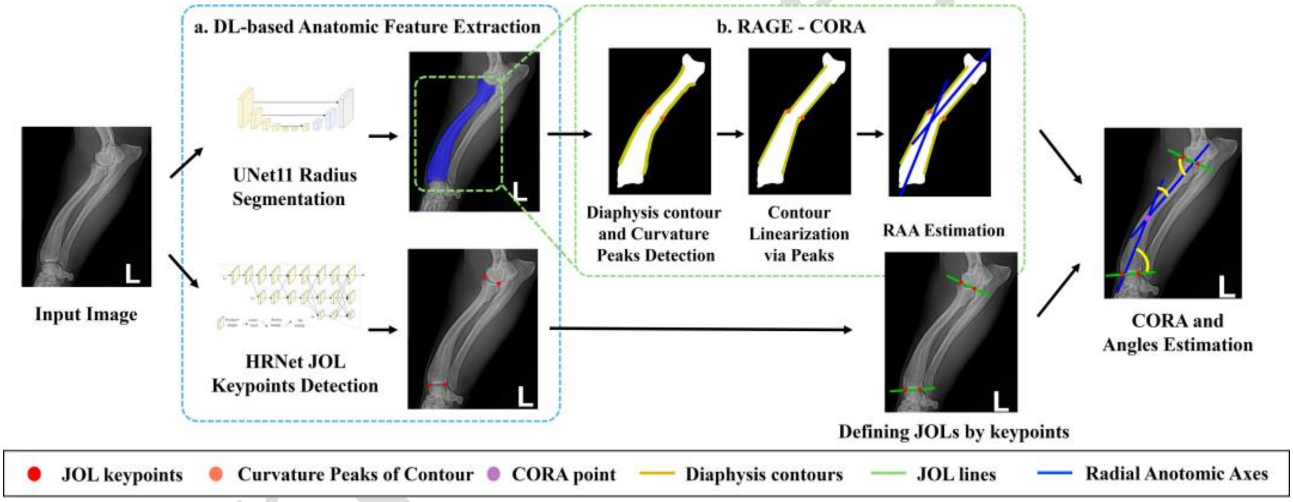

Fig. 3: Method Overview. The proposed pipeline takes an input radiograph and proceeds as follows: (a) DL-based feature extraction: A U-Net11 segments the radius (blue mask) while an HRNet pinpoints the JOL keypoints (red dots). (b) Segmentation-driven anatomical axis detection: From that mask, the diaphyseal contour (golden lines) is extracted and its curvature "peaks" (orange dots) identified. Each peak splits the contour into proximal and distal halves, which are then linearized and fittedyielding the proximal and distal radial anatomic axes (blue lines). Using the JOL keypoints from (a), JOL lines (green lines) are constructed, and by intersecting the proximal and distal RAAs obtained in (b), the CORA (purple dot) is determined enabling final angle estimation.

Radius Segmentation: We employed a U-Net11 model with a VGG11 encoder pre-trained on ImageNet for radius segmentation (Fig. 3) (Deng *et al.*, 2009). U-Net used an encoder-decoder architecture that integrated multi-scale context and preserved fine spatial detail through skip connections, thereby enabling precise boundary delineation in medical imaging (Ronneberger *et al.*, 2015). The VGG11 encoder pretrained on a large dataset enhanced learning efficiency even with small datasets (Simonyan & Zisserman, 2015). We applied data augmentation techniques to improve robustness across diverse species' radius anatomies. Segmentation performance was evaluated using intersection over union (IoU) and dice similarity score, with the dice score providing more intuitive accuracy assessment for medical image analysis (Müller *et al.*, 2022).

$$IoU = \frac{|A \cap B|}{|A \cup B|} = \frac{TP}{TP + FP + FN}$$

$$DSC = \frac{2|A \cap B|}{|A| + |B|} = \frac{2TP}{2TP + FP + FN}$$

We defined A as the set of pixels predicted as foreground and B as the set annotated as foreground in the reference masks; |·| denoted set cardinality. At the pixel level, true positives (TP), false positives (FP), and false negative (FN) were counted as $|A \cap B|, |A \setminus B|, and$ $|B \setminus A|$, respectively.

JOL Keypoint Detection: In this study, we estimated four anatomical keypoints using a deep learning-based model to predict proximal and distal JOLs. We adopted the High-Resolution Network (HRNet), which preserves high-resolution representations while learning multi-scale features (Sun *et al*., 2019) (Fig. 3). HRNet fused multiresolution feature maps during training for accurate keypoint localization. The model predicted 2D Gaussian heat maps representing spatial probability distributions, which enhanced detection performance and interpretability. This approach enabled localization of anatomical landmarks in radiographic X-ray images. The four detected key points defined the proximal and distal JOLs, which with the estimated RAA, were used to calculate six anatomical angles. The keypoint detection performance was evaluated using the NME, defined as follows (Yu *et al*., 2013).

$$NME = \frac{1}{m}\sum_{i=1}^{m}\frac{\|\widehat{p_i}-p_i\|_2}{\sqrt{height\cdot width}} \quad (1)$$

where $\widehat{p_i}$ and p_i denote the predicted and ground truth coordinates of the i-th keypoint, respectively, m is the total number of keypoints. The Euclidean distance between predicted and ground-truth keypoints was normalized by the geometric mean of image dimensions, which provided scale-invariant error relative to image size. Compared to face landmark detection, where bounding boxes were often used due to varying ROI sizes, the ROI in radiographs was relatively fixed, allowing normalization using the full image dimensions. The predicted proximal and distal JOLs were compared with ground-truth JOLs by measuring angular deviations to evaluate alignment with expert radiologists' definitions.

Segmentation-based CORA estimation: RAGE-CORA quantitatively estimated the CORA using anatomical geometry of the segmented radius (Fig. 3). To estimate CORA from the radius mask, the algorithm determined proximal and distal RAAs independently. The RAA passed through the radial bone shaft center, which required division into proximal and distal regions. This was achieved by analyzing the segmented radius contour and identifying bone-shaft regions through curvature analysis. A moving window approach computed curvature variation along the contour, separating low-curvature shaft regions from high-curvature areas. The medial, lateral, cranial, and caudal shaft contours were extracted in frontal and sagittal planes. The point of greatest curvature change divided each shaft into proximal and distal segments. Linear regression approximated segments as straight lines, and central axes defined the RAAs. The CORA was defined at the RAAs intersection, enabling quantitative, annotation-free estimation based on geometric rules.

Evaluation of estimated CORA using Mahalanobis OKS: Object Keypoint Similarity (OKS) evaluated predicted keypoint accuracy in image-based pose estimation by measuring similarity between predicted and ground-truth 2D coordinates (Lin *et al*., 2014). OKS computed the average normalized Euclidean distances between predicted and ground-truth keypoints, normalized to object scale, and provided a more robust evaluation metric than Euclidean distance alone.

$$OKS = \frac{\sum_i exp\left(-\frac{d_i^2}{2s^2k_i^2}\right)\delta(v_i > 0)}{\sum_i \delta(v_i > 0)} \quad (2)$$

where d_i is the Euclidean distance between the predicted and ground-truth locations of the i-th keypoint, s denotes the object scale, and k_i is a normalization factor specific to the i-th keypoint. The indicator function $\delta(v_i > 0)$ equals 1 if the i-th keypoint is visible (i.e., labeled), and 0 otherwise. However, since OKS is based on Euclidean distance, it does not account for anatomical structure, which poses a limitation when evaluating keypoints such as CORA on long bones like the radius. This may lead to inaccurate similarity measurements in such contexts. To address this issue, we proposed Mahalanobis OKS (MOKS), which replaced the Euclidean distance in the OKS formulation with the Mahalanobis distance to better reflect anatomical variations and structural context.

$$MOKS = exp\left(-(\hat{p}-p)^T\Sigma^{-1}(\hat{p}-p)\right) \quad (3)$$

where $\hat{p}$ and p represent the predicted and reference CORA points, respectively, and Σ denotes the covariance matrix computed from the pixel coordinates of the segmented radius mask.

$$\Sigma = \frac{1}{N-1}\sum_{i=1}^{N}[x_i - \bar{x} \;\; y_i - \bar{y}]^T \, [x_i - \bar{x} \;\; y_i - \bar{y}]$$

where (x_i, y_i) denotes the coordinates of each pixel within the segmented radius mask, and $(\bar{x}, \bar{y})$ represents their centroid. Since MOKS evaluates a single visible CORA point, it can be simplified into an exponential function of the Mahalanobis distance, as shown above. MOKS inherently accounted for object size through the covariance matrix of the radius mask coordinates used in the Mahalanobis distance calculation. As an exponential function, MOKS yielded values in the range of 0 to 1, where higher similarity results in values closer to 1, and lower similarity resulted in values closer to 0.

Statistical analysis: To compare the mean values of six angular measurements obtained from the left and right limbs of each subject between the chondrodystrophic and non-chondrodystrophic groups, Welch's t-test was applied. Due to the relatively limited sample size, the assumptions of normality and homoscedasticity could not be reasonably guaranteed, making Welch's test more appropriate than the conventional Student's t-test (Delacre *et al*., 2017). To avoid violation of independence due to correlation between left and right limb measurements within the same subject, the average of the left and right limb values was used as the representative value for each subject. Welch's t-test was performed as a two-tailed test, and statistical significance was set at $P<0.05$. To enhance the reliability of the statistical testing, permutation tests were additionally employed. These non-parametric tests do not rely on distributional assumptions and thus served to validate the robustness of the Welch's t-test findings (Good, 2005). Each permutation test was conducted with 10,000 iterations to ensure stable inference.

Inter-observer reliability was assessed using the angular measurements independently obtained by five veterinarians. The intraclass correlation coefficient (ICC) for a single measurement was calculated using a two-way random-effects model with absolute agreement ICC(2,1). For each angular measurement, a linear mixed-effects model was specified as follows, in order to appropriately address the intra-subject correlation caused by repeated left and right limb measurements.

$$\mathrm{Y}_{\mathrm{i,s,j}} = \mu + \mathrm{u}_{\mathrm{i}} + \mathrm{v}_{\mathrm{i,s}} + \mathrm{r}_{\mathrm{j}} + \mathrm{e}_{\mathrm{i,s,j}}$$

where i denotes the subject, $s \in \{L, R\}$ the limb (left and right) and j the evaluating veterinarian. μ represents the overall mean and u_i follows a normal distribution with mean zero and variance σ_u^2 representing the random intercept that accounts for between-subject variability. $v_{i,s}$ is normally distributed with mean zero and variance, capturing the variance σ_v^2 component associated with left–right differences within individual subjects. The rater effect, denoted as r_j is modeled as a normally distributed random effect with mean zero and variance σ_r^2, reflecting inter-rater variability. Finally, the residual error term $e_{i,s,j}$ is assumed to follow a normal distribution with mean zero and variance σ_e^2, representing the unexplained variance at the measurement level. Accordingly, ICC(2,1) was defined as:

$$\mathrm{ICC}(2,1) = \frac{\sigma_{\mathrm{u}}^2 + \sigma_{\mathrm{v}}^2}{\sigma_{\mathrm{u}}^2 + \sigma_{\mathrm{v}}^2 + \sigma_{\mathrm{r}}^2 + \sigma_{\mathrm{e}}^2}$$

The interpretation of ICC values is as follows: values greater than 0.75 indicate good reliability, whereas values exceeding 0.90 indicate excellent reliability (Koo & Li, 2016). Using the same approach, we further constructed a consensus by averaging the angular measurements obtained by the five veterinarians, and assessed the agreement between this consensus and the proposed method using ICC (2,1).

RESULTS

The proposed CORA estimation method was validated through analyses of deep learning models, comparisons between AI-based and expert consensus CORA, and measurements of radial deformity parameters. The time efficiency of AI-based estimation was compared with manual measurements by veterinarians to assess clinical applicability.

Deep learning model performance of radius segmentation and keypoint detection: For radius segmentation, 176 frontal and 199 sagittal images were used for training, with 40 shared test dataset for both planes. Input images were resized to 512×512 pixels. Data augmentation techniques such as random affine transformation, cropping, flipping, and Gaussian blur were applied. The U-Net11 model was trained with a batch size of 16, a learning rate of 0.0001, and 100 epochs, using Binary CrossEntropy loss function. The segmentation model performed with excellent accuracy, exceeding 0.9 across metrics, with IoU/DSC of 0.926/0.961 for frontal and 0.919/0.958 for sagittal (Fig. 4).

For keypoint detection, images were resized to 192×256 pixels with random rotation and horizontal flipping. The HRNet model was trained with a batch size of 32, a learning rate of 0.001, and 200 epochs, using Mean Squared Error loss function. The NME was 0.0061 in frontal and 0.0047 in sagittal planes (Fig. 4).

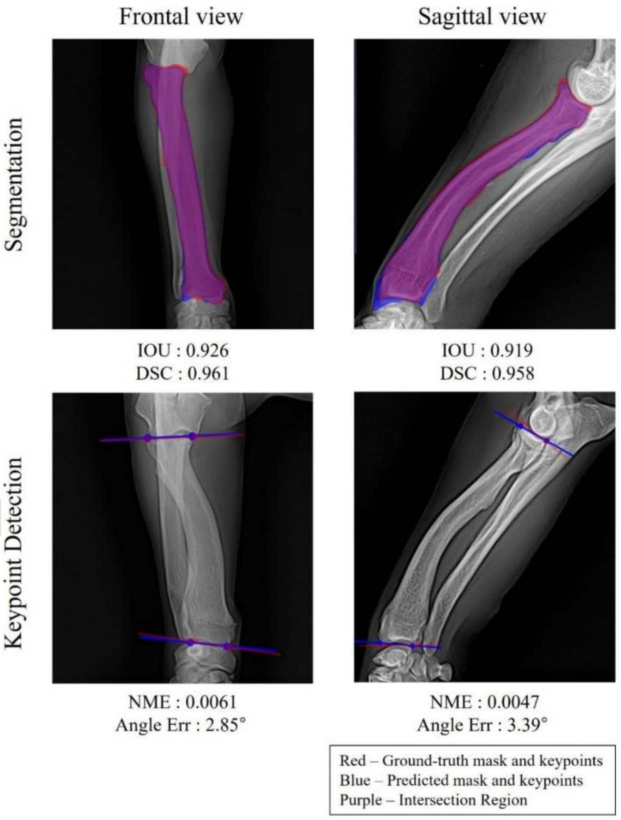

Fig. 4: Frontal (left) and sagittal (right) results in a 2×2 grid: top row shows segmentation overlays; bottom row shows key point detections. The deep learning model performance was evaluated using the Intersection over Union (IoU), Dice Similarity Coefficient (DSC), and Normalized Mean Error (NME), which are displayed within each panel. Overlays use red for ground-truth, blue for prediction, and purple for intersection. Performance metrics are listed below each panel, and the legend at lower right defines the color/marker scheme. Segmentation inputs were resized to 512×512 pixels, and keypoint detection inputs to 192×256 pixels with random rotation and horizontal flipping.

Comparative analysis of AI-based and manual CORA estimation by veterinarians: We compared AI-based CORA estimation with manual measurements by veterinarians. Mahalanobis Object Keypoint Similarity (MOKS) was used as the evaluation metric, with the expert consensus serving as the reference standard (Table 3). The proposed method showed lower overall MOKS scores than veterinarians for the entire population, but demonstrated a similar pattern of results. In both the frontal and sagittal plane, the proposed method showed higher MOKS scores in chondrodystrophic group than non-chondrodystrophic group. veterinarians tended to have lower scores in chondrodystrophic cases than in non-chondrodystrophic cases in the frontal plane. The standard deviation of MOKS among veterinarians was higher in the frontal plane than in the sagittal plane, indicating lower inter-observer consensus.

Table 3: MOKS between estimated by proposed method and the annotated CORA (Manual)

	Non-chondrodystrophic breed (SD)	Chondrodystrophic breed (SD)	Total (SD)
Frontal (Manual)	0.783 (0.100)	0.771 (0.106)	0.777(0.103)
Frontal (Proposed)	0.636	0.793	0.715
Sagittal (Manual)	0.842 (0.072)	0.879 (0.061)	0.861(0.066)
Sagittal (Proposed)	0.796	0.841	0.819

SD, standard deviation

Presentation of six angle measurements: Table 4 shows six angle measurements from both our method and manual assessments, grouped by breed type. The results highlight distinct anatomical differences between chondrodystrophic and non-chondrodystrophic breeds, with the divergence being most evident in FIA and SIA. Table 5 further refines these findings by presenting values for each breed individually, thereby providing more detailed reference data than the broader comparisons of chondrodystrophic versus non-chondrodystrophic or retriever versus non-retriever breeds reported in previous studies.As shown in Table 6, both Welch's t-test and permutation tests indicated that FIA, MPRA, and SIA showed significant differences between the two breed groups (P<0.05), whereas LDRA, CrPRA, and CdDRA did not demonstrate statistically significant differences (P>0.05). These trends matched the manual measurements, showing strong agreement with expert assessments.

Table 4: Angle comparison between veterinarian-measured consensus and proposed method

		Non-chondrodystrophic breed	Chondrodystrophic breed	Total
FIA	Manual	8.5±3.2	16.7±8.9	12.6±7.8
	Proposed	5.2±3.2	15.6±7.2	10.4±7.6
MPRA	Manual	82.6±4.2	67.4±13.2	75.0±12.4
	Proposed	83.7±5.0	66.7±12.2	75.2±12.6
LDRA	Manual	82.0±6.5	79.9±8.1	80.9±7.3
	Proposed	81.5±6.9	81.0±6.6	81.3±6.7
SIA	Manual	12.1±5.5	26.2±5.7	19.1±9.1
	Proposed	10.6±4.6	23.0±4.7	16.8±7.8
CrPRA	Manual	38.2±21.8	26.0±19,7	32.1±21.4
	Proposed	38.1±20.1	26.3±18.7	32.2±20.1
CdDRA	Manual	67.5±16.4	70.4±16.1	68.9±16.1
	Proposed	67.3±14.7	72.2±15.4	69.7±15.0

Values are expressed as mean±standard deviation (SD) with 95% confidence intervals (CI). FIA, Frontal Intersection Angle; MPRA, Medial Proximal Radial Angle; LDRA, Lateral Distal Radial Angle; SIA, Sagittal Intersection Angle; CrPRA, Cranial Proximal Radial Angle; CdDRA, Caudal Distal Radial Angle. Values are expressed as mean±standard deviation (SD).

Table 7 presents Intraclass Correlation Coefficient (ICC) results for angular measurements obtained by five veterinarians. All ICC values were computed by specifying linear mixed-effects models in Python using the *statsmodels* library. For the overall population, the veterinarians' ICC values were above 0.75 for all angular measurements, indicating high agreement; however, in the non-chondrodystrophic group, FIA and MPRA showed lower levels of agreement. The proposed method showed ICC values above 0.8 for all angular measurements, thus demonstrating good to excellent agreement with expert consensus, as presented in Table 8. FIA and MPRA showed lower ICCs in non-chondrodystrophic dogs than chondrodystrophic dogs, matching the inter-veterinarian trend. The proposed method's agreement with expert consensus followed patterns similar to inter-veterinarian agreement, achieving high consistency in angles with strong inter-rater agreement, and lower consistency in anatomically ambiguous cases. All ICC results yielded p-values below 0.0001, indicating that statistical significance was secured. Beyond accuracy, computational speed was also evaluated.

Table 5: Breed-specific angle measurements using the proposed method

Breed	FIA	MPRA	LDRA	SIA	CrPRA	CdDRA
Maltese (17)	5.2 ± 2.9	83.3 ± 5.1	82.6 ± 7.9	13.5 ± 1.9	38.4 ± 18.7	76.7 ± 7.8
Dachshund (8)	19.0 ± 3.5	60.5 ± 10.5	80.4 ± 4.7	20.6 ± 5.8	25.3 ± 16.8	76.9 ± 15.1
Welsh Corgi (22)	20.1 ± 6.4	59.2 ± 5.5	80.3 ± 9.4	22.9 ± 3.3	22.4 ± 15.3	73.7 ± 12.4
Pekingese (6)	8.1 ± 2.7	81.4 ± 5.9	80.2 ± 6.4	26.6 ± 4.6	15.0 ± 2.4	76.6 ± 11.5
French Bulldog (3)	6.8 ± 5.1	78.8 ± 1.9	86.2 ± 1.0	23.5 ± 2.8	63.3 ± 3.5	44.8 ± 1.9
Spitz (3)	4.8 ± 0.9	82.0 ± 8.7	86.3 ± 3.2	5.1 ± 0.9	44.1 ± 13.3	64.9 ± 17.2
Mixed (12)	1.6 ± 1.8	85.5 ± 6.3	69.2 ± 9.0	11.7 ± 4.0	58.7 ± 5.1	80.6 ± 6.5
Bichon Frise (4)	7.8 ± 4.5	82.2 ± 0.1	85.2 ± 2.5	18.6 ± 1.6	15.5 ± 4.3	60.7 ± 2.6
Poodle (14)	1.6 ± 1.8	85.5 ± 2.0	80.3 ± 4.6	8.0 ± 0.0	18.7 ± 19.9	49.7 ± 11.4
Pomeranian (15)	8.0 ± 2.4	84.6 ± 4.1	80.6 ± 4.1	10.0 ± 2.9	42.6 ± 25.8	65.7 ± 17.8
Total	5.2 ± 2.9	83.3 ± 5.1	82.6 ± 7.9	13.5 ± 1.9	38.4 ± 18.7	76.7 ± 7.8

Values are expressed as mean ± standard deviation (SD).

Table 6: Results of Welch's t-test and permutation tests for angular measurements

		Welch's t-statistic	p-value (Welch's t-test)	p-value (permutation test)
FIA	Manual	2.92	0.0165	0.0045
	Proposed	4.21	0.0017	0.0003
MPRA	Manual	-3.79	0.0041	0.0001
	Proposed	-4.37	0.0013	0.0001
LDRA	Manual	-0.796	0.438	0.447
	Proposed	-0.222	0.828	0.824
SIA	Manual	5.70	0.00003	0.0010
	Proposed	5.90	0.00002	0.0001
CrPRA	Manual	-1.32	0.208	0.207
	Proposed	-1.39	0.185	0.185
CrDRA	Manual	0.425	0.677	0.674
	Proposed	0.759	0.459	0.454

Manual and proposed results were calculated using the same datasets (n = 176 for FIA, MPRA, and LDRA; n = 199 for SIA, CrPRA, and CdDRA).

Table 7: ICC (2,1) among five veterinarians for angle measurements

	Non-chondrodystrophic breed	Chondrodystrophic breed	Total
FIA	0.370	0.834	0.805
MPRA	0.695	0.911	0.950
LDRA	0.921	0.901	0.907
SIA	0.834	0.768	0.913
CrPRA	0.789	0.834	0.788
CrDRA	0.863	0.890	0.882

Time efficiency of the proposed CORA estimation method: The proposed method required 1.19 seconds per image for CORA and angular estimation using GPU inference, including 1.17 seconds for segmentation and keypoint detection inference, and 0.2 seconds for RAGE-CORA and measurements. An experienced veterinarian needed 24 seconds, including 3 seconds for keypoint selection, 10 seconds for RAA estimation, 1 second for CORA localization, and 10 seconds for measurements. Non-expert users required approximately 5.5 minutes (3–8 minutes). We did not conduct statistical testing; therefore, no firm conclusion about speed can be drawn. The observed timings suggest a potential time saving, particularly for non-experts.

Table 8: ICC (2,1) between veterinarian-measured consensus and proposed method for angle measurements

	Non-chondrodystrophic breed	Chondrodystrophic breed	Total
FIA	0.268	0.908	0.876
MPRA	0.571	0.838	0.858
LDRA	0.837	0.823	0.818
SIA	0.920	0.726	0.928
CrPRA	0.901	0.836	0.831
CrDRA	0.925	0.853	0.922

DISCUSSION

This study confirmed the high accuracy and performance of AI-based radial segmentation and keypoint detection across frontal and sagittal radiographic planes. The AI predictions of the CORA point closely matched those of the five veterinarians, especially in chondrodystrophic dogs, where ALDs are more prevalent than in non-chondrodystrophic breeds. The advantages of AI include fast processing, high precision, and reduced interobserver variation. These results support the applicability of AI as a reliable aid in clinical diagnosis.

The accuracy of CORA prediction was relatively low in non-chondrodystrophic dogs and in the frontal plane. CORA prediction accuracy was lower in non-chondrodystrophic dogs and in the frontal plane, likely because minimal radial curvature in these settings causes the proximal and distal RAAs to run nearly parallel, making their intersection highly sensitive to small measurement variations. The lower ICC of the FIA angle in non-chondrodystrophic dogs, observed by both veterinarians and the proposed method, was presumed to result from the same cause. In contrast, chondrodystrophic dogs and sagittal views exhibited greater radial curvature, allowing clearer RAA intersections and improved prediction performance.

Prior angular measured for evaluating ALDs include FPA and SPA (Fox *et al*., 2006; Knapp *et al*., 2016). Building on these, this study evaluated the intersection angle (θ) between the proximal and distal RAAs and further proposed FIA and SIA as additional indicators. Both the FIA and SIA represent the intersection angle between the proximal and distal RAAs and directly reflect changes in radial curvature. SIA is conceptually equivalent to the intersection angle (θ) described in earlier studies for the sagittal plane and based on the reference values established in this study, increased SIA may be interpreted as procurvatum or recurvatum, respectively (Knapp *et al*., 2016). Similarly, FIA values that exceed the normal range may indicate valgus or varus deformities. These angles offer a more intuitive interpretation than conventional formula-based approaches, and may prove to be objective and clinically relevant parameters in future studies involving dogs with ALDs.

In addition to these angular parameters, this study introduced the Mahalanobis Object Keypoint Similarity (MOKS) as a novel metric for evaluating CORA estimation. Unlike OKS, which requires normalization for object scale and is based solely on Euclidean distance, MOKS inherently incorporates the covariance structure of the radius, allowing anatomically informed similarity assessment (Fig. 5). This provides a distinct advantage in the evaluation of long bone structures such as the radius.

Although the proposed model showed similar accuracy to veterinarians in estimating the CORA point, several limitations must be acknowledged. The CORA point lacks a clearly defined ground truth, which makes it difficult to objectively assess the accuracy of the deep learning model. The reliability of the AI was indirectly evaluated by comparing its predictions with the manual measurements made by veterinarians.

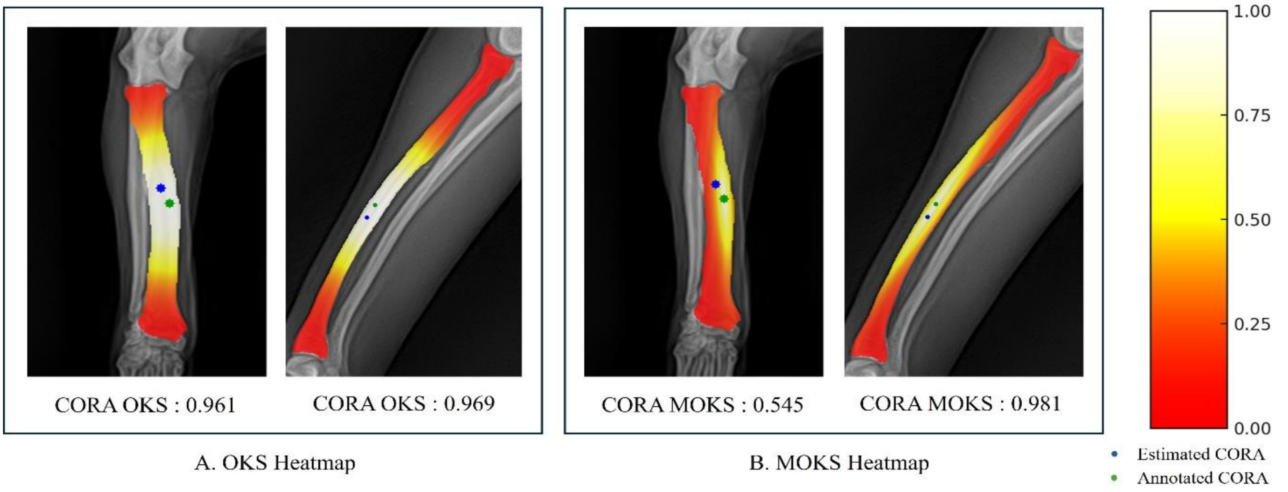

A. OKS Heatmap

B. MOKS Heatmap

Fig. 5: This figure illustrates a comparison between OKS and MOKS heat maps at the estimated CORA positions relative to the annotated CORA. The heatmaps use a red-to-white colormap—lower OKS/MOKS values in red, higher values in whitewith annotated CORA marked by green dots and predicted CORA by blue dots.

In the frontal plane, when the medial coronoid process of the ulna was obscured due to an overlap with the radius, the medial aspect of the radius was used as a substitute point. However, the deep learning model encountered difficulties in accurately distinguishing between such exceptions. Consequently, the accuracy of this specific key point is reduced, indicating the need for further model improvement by including more exceptional cases during training.

Cases with biapical or multiapical deformities in which more than one CORA point was identified during the preliminary evaluation were excluded. Consequently, the current model is not applicable to complex deformities involving multiple CORA points. Further studies are required to extend the model's applicability to such cases.

This study relied on physical examinations and orthogonal radiography for orthopedic assessment. Torsional deformities exceeding 15° could compromise measurement accuracy, potentially causing errors of over 5° in the frontal plane (Piras *et al.*, 2012; Kroner *et al.*, 2017). Since radiographs alone cannot clearly detect torsion, their impact may have been underestimated in certain cases. Therefore, the average joint angles for chondrodystrophic breeds should be considered provisional. Future research incorporating 3D CT analysis is recommended.

With the growing need for automated evaluation, recent studies in veterinary and human medicine have increasingly applied AI to appendicular skeletal analyses. In veterinary science, deep learning has been used to measure the TPA angle and develop diagnostic models for canine patellar joint diseases (Tonima *et al.*, 2021; Shim *et al.*, 2023). In human medicine, studies have proposed deep learning-based landmark recognition and angle measurement for lower limb alignment, as well as fully automated models for detecting landmarks in weight-bearing lateral foot radiographs (Ryu *et al.*, 2022; Jo *et al.*, 2023). Additionally, an automated measurement of the hip-knee-ankle angle using deep learning has been developed and validated, demonstrating its high reliability and validity in clinical settings (Pei *et al.*, 2021).

In conclusion, this study demonstrated that an AI-based approach can be used to identify the CORA point and six angular parameters (FIA, MPRA, LDRA, SIA, CrPRA, CdDRA) from canine forelimb radiographs, offering valuable support in the diagnosis and surgical planning of ALDs. Compared with veterinarians, AI provides faster diagnosis, achieves expert-level accuracy, reduces inter-observer variability, and enhances clinical efficiency. This framework lays the groundwork for AI-assisted surgical planning in veterinary orthopedics.

Conflict of interest: The authors declare that this study was conducted in the absence of any commercial or financial relationships that could be construed as potential conflicts of interest.

Ethics statement: The animal study protocol was reviewed and approved by the Institutional Animal Care and Use Committee of Jeonbuk National University (approval no. JBNU 2023-168).

Funding: No funding was received for this study.

Abbreviations: CORA (Center of Rotation of Angulation); CT (Computed Tomography); JOL (Joint Orientation Line); RAA (Radial Anatomical Axes); MPRA (Medial Proximal Radial Angle); LDRA (Lateral Distal Radial Angle); FIA (Frontal Intersection Angle); CrPRA (Cranial Proximal Radial Angle); CdDRA (Caudal Distal Radial Angle); SIA (Sagittal Intersection Angle).

Acknowledgments: The authors thank all the veterinarians and colleagues in the Department of Veterinary Medical Imaging, College of Veterinary Medicine, Jeonbuk National University, and the animal medical centers that participated in this study for their assistance in collecting data and writing this manuscript.

Author Contributions: SR, TH, HG and HY conceived, designed and drafted the manuscript. SR and TH acquired the data. SH, HC, KL, and HY analyzed and interpreted the data. All authors contributed to and approved the submitted manuscript.

Data availability statement: The original data presented in this study are included in the article. Further inquiries may be directed to the corresponding author.

REFERENCES

Delacre M, Lakens D, Leys C, 2017. Why psychologists should by default use Welch's t-test instead of Student's t-test. IRSP30:92–101.

Deng J., Dong W., Socher R., *et al.*, 2009. ImageNet: A large-scale hierarchical image database. IEEE 248–255.

Dismukes DI, Fox DB, Tomlinson JL, *et al.*, 2008. Use of radiographic measures and three-dimensional computed tomographic imaging in surgical correction of an antebrachial deformity in a dog. J Am Vet Med Assoc 232:68-73.

Duncan KL, Mielke BA, Phillips A, *et al.*, 2022. Assessment of normal radial joint orientation angles in nonchondrodystrophic small-breed dogs. J Am Vet Med Assoc 261:1-4.

Fasanella F, Tomlinson J, Welihozkiy A, *et al.*, 2010. Radiographic measurements of the axes and joint angles of the canine radius and ulna. Vet Comp Orthop Traumatol 23:A11.

Fox D and Tomlinson J, 2012. Principles of angular limb deformity correction. Vet Surg: Small Animal 1:657-668.

Fox DB, 2010. CORA method of planning corrective osteotomies as applied to veterinary orthopedics. In: WVOC 2010, Bologna (Italy), 15-18 set. 2010.

Fox DB, Tomlinson JL, Cook, *et al.*, 2006. Principles of uniapical and biapical radial deformity correction using dome osteotomies and the center of rotation of angulation methodology in dogs. Vet Surg 35:67-77.

Good PI, 2005. Permutation, Parametric, and Bootstrap Tests of Hypotheses. 3rd ed. Springer, New York.

Ronneberger O, Fischer P,, Brox T. 2015. U-Net: Convolutional networks for biomedical image segmentation. 2015 International Conference on Medical Image Computing and Computer-Assisted Intervention (MICCAI), Springer, 234–241.

Jo C, Hwang D, Ko S, *et al.*, 2023. Deep learning-based landmark recognition and angle measurement of full-leg plain radiographs can be adopted to assess lower extremity alignment. KSSTA31:1388–97.

Kim SY, Snowdon KA, Decamp CE, 2017. Single oblique osteotomy for correction of antebrachial angular and torsional deformities in a dog. J Am Vet Med Assoc 251:333–9.

Knapp JL, Tomlinson JL, Fox DB, 2016. Classification of angular limb deformities affecting the canine radius and ulna using the center of rotation of angulation method. Vet Surg 45:295–302.

Kranenburg H-JC, Grinwis GC, Bergknut N, *et al.*, 2013. Intervertebral disc disease in dogs–Part 2: Comparison of clinical, magnetic resonance imaging, and histological findings in 74 surgically treated dogs. Vet J 195:164–71.

Kroner K, Cooley K, Hoey S, *et al.*, 2017. Assessment of radial torsion using computed tomography in dogs with and without antebrachial limb deformity. Vet Surg 46:24–31.

Koo TK, Li MY, 2016. A guideline of selecting and reporting intraclass correlation coefficients for reliability research. J Chiropr Med 15(2), 155–163.

Kwon M, Kwon D, Lee J, *et al*., 2022. Evaluation of the radial procurvatum using the center of rotation of angulation methodology in chondrodystrophic dogs. Front Vet Sci 8:774993.

Lin TY, Maire M, Belongie S, *et. al*., 2014. Microsoft COCO: Common objects in context. 2014 European Conference on Computer Vision (ECCV), Springer, 740–755.

Marcellin-Little D, 2020. Limb deformities in dogs: the role of the primary care veterinarian. Illinois State Veterinary Medical Association.

Müller D, Soto-Rey I, Kramer F, 2022. Towards a guideline for evaluation metrics in medical image segmentation. BMC Res Notes 15:210.

Muniyya NC, 2023. Clinical studies on angular limb deformities of antebrachiam in dogs. Sri Venkateswara Veterinary University.

Parker HG, Vonholdt BM, Quignon P, *et al*., 2009. An expressed fgf4 retrogene is associated with breed-defining chondrodysplasia in domestic dogs. Science 325:995–8.

Pei Y, Yang W, Wei S, *et al*., 2021. Automated measurement of hip–knee–ankle angle on the unilateral lower limb X-rays using deep learning. Phys Eng Sci Med 44:53–62.

Piras LA, Peirone B, Fox D, 2012. Effects of antebrachial torsion on the measurement of angulation in the frontal plane: a cadaveric radiographic analysis. Vet Comp Orth Traumatol 25:89–94.

Pulkkinen HS, Reunanen VL, Hyytiæinen HK, *et al*., 2020. The intra-and intertester repeatability of radiographic elbow incongruity grading is high in chondrodystrophic dog breeds. Vet Radiol Ultrasound 61:329–35.

Ryu SM, Shin K, Shin SW, *et al*., 2022. Automated landmark identification for diagnosis of the deformity using a cascade convolutional neural network (FlatNet) on weight-bearing lateral radiographs of the foot. Comp Biol Med 148:105914.

Simonyan K, Zisserman A, 2015. Very deep convolutional networks for large-scale image recognition. 3rd International Conference on Learning Representations (ICLR)

Shim H, Lee J, Choi S, *et al*., 2023. Deep learning-based diagnosis of stifle joint diseases in dogs. Vet Radiol Ultrasound 64:113–22.

Smolders LA, Bergknut N, Grinwis GC, *et al*., 2013. Intervertebral disc degeneration in the dog. Part 2: chondrodystrophic and non-chondrodystrophic breeds. Vet J 195:292–9.

Sun K, Xu B, Li J, *et al*., 2019. Deep high-resolution representation learning for human pose estimation. 2019 IEEE/CVF Conference on Computer Vision and Pattern Recognition (CVPR), IEEE, 5686–5696.

Tonima MA, Hossain FA, Dehart, *et al*., 2021. Auto-Detection of Tibial Plateau Angle in Canine Radiographs Using a Deep Learning Approach. 2021 IEEE 10th Data Driven Control and Learning Systems Conference (DDCLS): 468–72.

Yu X, Huang J, Zhang S, *et al*., 2013. Pose-free facial landmark fitting via optimized part mixtures and cascaded deformable shape model. 2013 IEEE International Conference on Computer Vision (ICCV), IEEE, 1944–1951.